Supplementary Information: Observation of a Floquet symmetry-protected topological phase with superconducting qubits

Xu Zhang[1,*], Wenjie Jiang[2,*], Jinfeng Deng[1,*], Ke Wang[1], Jiachen Chen[1], Pengfei Zhang[1], Wenhui Ren[1], Hang Dong[1], Shibo Xu[1], Yu Gao[1], Feitong Jin[1], Xuhao Zhu[1], Qiujiang Guo[4,3], Hekang Li[1,3], Chao Song[1,3], Alexey V. Gorshkov[5], Thomas Iadecola[6,7], Fangli Liu[5,8], Zhexuan Gong[9,10], Zhen Wang[1,3,†], Dong-Ling Deng[2,11,‡], and H. Wang[1,3,4]

[1] *Interdisciplinary Center for Quantum Information, State Key Laboratory of Modern Optical Instrumentation, and Zhejiang Province Key Laboratory of Quantum Technology and Device, Department of Physics, Zhejiang University, Hangzhou 310027, China*
[2] *Center for Quantum Information, IIIS, Tsinghua University, Beijing 100084, China*
[3] *Alibaba-Zhejiang University Joint Research Institute of Frontier Technologies, Hangzhou 310027, China*
[4] *Hangzhou Global Scientific and Technological Innovation Center, Zhejiang University, Hangzhou 311215, China*
[5] *Joint Quantum Institute and Joint Center for Quantum Information and Computer Science, University of Maryland and NIST, College Park, MD, USA*
[6] *Department of Physics and Astronomy, Iowa State University, Ames, Iowa 50011, USA*
[7] *Ames Laboratory, Ames, Iowa 50011, USA*
[8] *QuEra Computing Inc., Boston, Massachusetts 02135, USA*
[9] *Department of Physics, Colorado School of Mines, Golden, Colorado 80401, USA*
[10] *National Institute of Standards and Technology, Boulder, Colorado 80305, USA*
[11] *Shanghai Qi Zhi Institute, 41th Floor, AI Tower, No. 701 Yunjin Road, Xuhui District, Shanghai 200232, China*

Here we provide more details on the theory of the Floquet symmetry-protected topological phase (Sec. I), on our numerical simulations (Sec. II), and on our experimental setup (Sec. III). We also provide additional experimental data (Sec. IV).

I. THEORETICAL UNDERSTANDING

A. Introduction to Floquet time crystals

In order to obtain a better intuitive understanding of the Floquet symmetry-protected topological (FSPT) phase, we first introduce the basic concepts behind Floquet time crystals and present a prototypical model as a concrete example.

Spontaneous symmetry breaking is an important concept in modern physics. It occurs when the steady state of a physical system does not respect the symmetries of the Hamiltonian governing this system. An important example that manifests spontaneous symmetry breaking is an ordinary crystal, which breaks the continuous spatial translation symmetry. More precisely, in a crystal, the state of the system, unlike its Hamiltonian, is not invariant under continuous translation operators. Analogously, systems that spontaneously break time-translation symmetry are named time crystals [S1, S2]. Although there is a no-go theorem for continuous time crystals at equilibrium [S3, S4], Floquet time crystals manifest themselves in many physical systems. There are two equivalent definitions of Floquet time crystals in Ref. [S5], which characterize this concept from the perspective of the expectation value of an operator and from the perspective of the eigenstates of the Floquet evolution unitary, respectively. The first definition states that time-translation symmetry breaking occurs if, for every short-range correlated state $|\psi(t)\rangle$ at arbitrary time t, there exists an operator O satisfying $\langle\psi(t+T)|\,O\,|\psi(t+T)\rangle \neq \langle\psi(t)|\,O\,|\psi(t)\rangle$, where $|\psi(t+T)\rangle = U_F(T)\,|\psi(t)\rangle$, with $U_F(T)$ the Floquet evolution unitary corresponding to one period T. This definition implies how to observe time crystals experimentally and is used in our paper. The second definition states that time-translation symmetry breaking occurs if all eigenstates of the Floquet evolution unitary are long-range correlated. This concept is used in our theoretical analysis.

To be more concrete, we introduce the following prototypical time-dependent Hamiltonian previously studied in Refs. [S5, S6] as an example of a Floquet time crystal:

$$H_F(t) = \begin{cases} H_1 = \pi/2 \sum_k \hat{\sigma}_k^x, & 0 < t < T_1, \\ H_2 = \sum_k J_k \hat{\sigma}_k^z \hat{\sigma}_{k+1}^z + h_k^z \hat{\sigma}_k^z, & T_1 < t < T, \end{cases} \tag{S1}$$

where J_k and h_k^z are uniformly chosen from the following intervals: $J_k \in [J/2, 3J/2]$ and $h_k^z \in [0, h^z]$. We set $T = 2T_1 = 2$. The Floquet evolution operator for one period can then be written as $U_F = \exp(-iH_2)\exp(-i\pi/2\sum_k \hat{\sigma}_k^x)$.

We consider eigenstates of H_2, which are product states in the computational z basis: $|\Theta\rangle = |\{s_k\}\rangle$ with $s_k = \pm 1$. Such states are easy to prepare experimentally. Since U_F has the effect, up to a global phase, of flipping all spins, the state $|\Theta\rangle$ is related to another state $|-\Theta\rangle = |\{-s_k\}\rangle$, which is also an eigenstate of H_2. Defining $E^+(\Theta)$ and $E^-(\Theta)$ via $\sum_k J_k \hat{\sigma}_k^z \hat{\sigma}_{k+1}^z |\Theta\rangle = E^+(\Theta)\,|\Theta\rangle$ and $\sum_k h_k^z \hat{\sigma}_k^z |\Theta\rangle = E^-(\Theta)\,|\Theta\rangle$, we have

$$U_F\,|\Theta\rangle = \exp[-i(E^+(\Theta) - E^-(\Theta))]\,|-\Theta\rangle\,, \tag{S2}$$

$$U_F\,|-\Theta\rangle = \exp[-i(E^+(\Theta) + E^-(\Theta))]\,|\Theta\rangle\,. \tag{S3}$$

Therefore, in the subspace formed by $|\pm\Theta\rangle$, U_F has the matrix

form

$$U_F = \begin{bmatrix} 0 & e^{-i(E^+(\Theta)-E^-(\Theta))} \\ e^{-i(E^+(\Theta)+E^-(\Theta))} & 0 \end{bmatrix}. \quad \text{(S4)}$$

Diagonalizing this matrix gives eigenvalues $\pm\exp(-iE^+(\Theta))$ and eigenstates $|\Theta\rangle \pm \exp[iE^-(\Theta)]\,|-\Theta\rangle$. The eigenstates of U_F are thus paired cat states with long-range correlations. Thus, this model satisfies the second definition of a Floquet time crystal in Ref. [S5], so discrete time-translation symmetry breaking occurs in this system. (Note that, in order for these correlations to be stable to perturbations, disorder in the couplings J_k and h_k^z that is sufficiently strong to render U_F many-body localized is required.) Futhermore, as the Floquet operator has eigenvalues $\pm\exp(-iE^+(\Theta))$, if we diagonalize the effective Hamiltonian of the Floquet operator, we will get two eigenvalues with quasi-energy difference π. This model therefore corresponds to the π-spin-glass phase introduced in Ref. [S7].

B. Our model: the FSPT phase

Unlike Floquet time crystals introduced above, the Floquet SPT phase breaks discrete time-translation symmetry only at the boundaries. To be specific, our model of the Floquet SPT phase exhibits subharmonic response at frequency $2\pi/2T$ only at the edges but not in the bulk of the system. Here T is the period of the Floquet driving. We will now present additional theoretical analysis of our model.

1. *Localized and SPT quantum states*

Our FSPT phase has two distinct governing Hamiltonians during different time intervals as shown in the main text. In the first time interval, this governing Hamiltonian H_1 is the sum of one-body Pauli operators on different sites. In the second time interval, the governing Hamiltonian H_2 includes interaction among neighboring sites, which introduces the subtle many-body properties in this system.

Let us begin by studying the static Hamiltonian H_2 [S8],

$$H_2 = -\sum_k \left[J_k \hat{\sigma}_{k-1}^z \hat{\sigma}_k^x \hat{\sigma}_{k+1}^z + V_k \hat{\sigma}_k^x \hat{\sigma}_{k+1}^x + h_k \hat{\sigma}_k^x\right], \quad \text{(S5)}$$

where the parameters are chosen as in the main text. This Hamiltonian has a $Z_2 \times Z_2$ symmetry, corresponding to $\hat{\sigma}_k^{z,y} \longrightarrow -\hat{\sigma}_k^{z,y}$ independently on even- or odd-numbered sites, i.e. $[H_2, \prod_k \hat{\sigma}_{2k}^x] = 0$ and $[H_2, \prod_k \hat{\sigma}_{2k+1}^x] = 0$. All three-body terms $S_k = \hat{\sigma}_{k-1}^z \hat{\sigma}_k^x \hat{\sigma}_{k+1}^z$ in H_2 commute with each other, i.e. $[S_k, S_l] = 0$, and are called stabilizers.

In the extreme case $V_k = h_k = 0$, the eigenstates of this Hamiltonian are the mutual eigenstates of all stabilizers and are called cluster states. They are SPT states with $Z_2 \times Z_2$ symmetry. The SPT phase manifests itself in the open-boundary case: there is one effective free spin at each end of the chain. The topological nature of the eigenstates is encapsulated by the string-order parameter:

$$O_{\rm st}(l,j) = \langle \hat{\sigma}_l^z \hat{\sigma}_{l+1}^y (\prod_{k=l+2}^{j-2} \hat{\sigma}_k^x) \hat{\sigma}_{j-1}^y \hat{\sigma}_j^z \rangle, \quad \text{(S6)}$$

which takes random values $O_{\rm st}(l,j) = \pm 1$ for different eigenstates and different disorder realizations. Thus, we can define a non-local analogue of the Edwards-Anderson glass-order parameter to characterize the FSPT phase: $O_{\rm sg} = [\![O^2(l,j)]\!]$, where $[\![]\!]$ denotes an average over sites, states, and random realizations. The entanglement spectra of the eigenstates are degenerate. This degeneracy can serve as another manifestation of the topological nature of the phase. Furthermore, in this limit, all energy levels are exactly four-fold degenerate. The corresponding degenerate eigenstates can be divided into four groups: $\{|A_k\rangle = |\uparrow \ldots \uparrow\rangle\}$, $\{|B_k\rangle = |\downarrow \ldots \uparrow\rangle\}$, $\{|C_k\rangle = |\uparrow \ldots \downarrow\rangle\}$, $\{|D_k\rangle = |\downarrow \ldots \downarrow\rangle\}$. Here we are working in the $\hat{\sigma}_z$ basis, and the two arrows represent the effective boundary spins and the ... denotes the bulk spins. These states are related by $\prod \hat{\sigma}_{\rm odd}^x |A_k\rangle = |B_k\rangle$, $\prod \hat{\sigma}_{\rm even}^x |A_k\rangle = |C_k\rangle$, $\prod \hat{\sigma}_{\rm all}^x |A_k\rangle = |D_k\rangle$, where $\prod \hat{\sigma}_{\rm even}^x \equiv \prod_k \hat{\sigma}_{2k}^x$, $\prod \hat{\sigma}_{\rm odd}^x \equiv \prod_k \hat{\sigma}_{2k+1}^x$, and $\prod \hat{\sigma}_{\rm all}^x \equiv \prod_k \hat{\sigma}_k^x$.

When $V_k,\ h_k \neq 0$, the one- and two-body terms make the eigenstates of this Hamiltonian depart from cluster states. However, if we keep the Hamiltonian deep in the topological phase (the phase we are interested in), i.e. $J_k \gg V_k, h_k$, we can also interpret this model from a many-body localized (MBL) perspective. Unlike the $V_k = h_k = 0$ Hamiltonian with strictly localized stabilizers as the integrals of motion, in the MBL phase, the system posses a set of mutually commuting quasi-local integrals of motion. Similarly, for open boundary conditions, there exists a quasi-local effective free spin at each edge, which contains bulk components decaying exponentially with the distance from the edge. In this case, the string-order parameter and the degeneracy of the entanglement spectra can still manifest the topological nature of the eigenstates. Moreover, while the energy spectrum is no longer exactly four-fold degenerate in a finite system, it is still nearly four-fold degenerate, and the corresponding eigenstates can still be divided into the four groups introduced above.

2. *The emergence of the FSPT phase*

Having reviewed the properties of the static Hamiltonian H_2, let us now consider the Floquet case, wherein we periodically drive the above SPT Hamiltonian as discussed in the

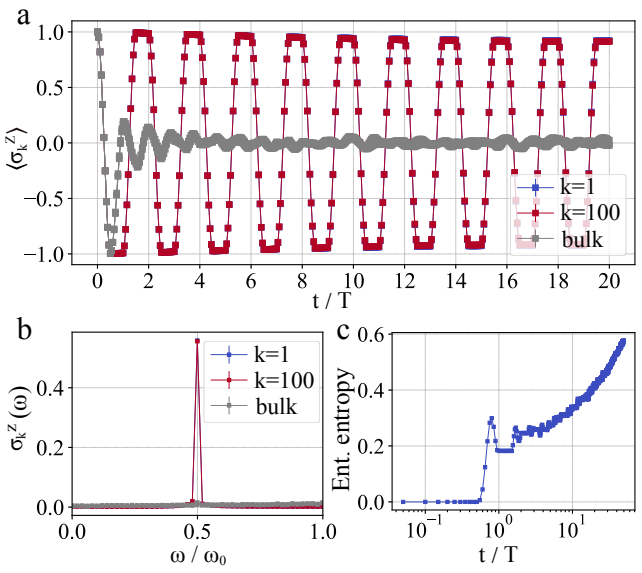

FIG. S1. The evolution of the FSPT phase for system size $L = 100$, computed using the time-evolving block decimation methods. Results shown here are averaged over 1000 random realizations, with parameters $J = \Delta J = 1$, $h = \Delta h = V = \Delta V = \delta = 0.05$. **a**. Time evolution of disorder-averaged local observables. For the edge spins, it is clear that $\langle\sigma_1^z\rangle$ and $\langle\sigma_{100}^z\rangle$ (which are right on top of each other, so that $k = 1$ is not visible) display persistent oscillations with $2T$ periodicity, manifesting the breaking of discrete time-translation symmetry. In stark contrast, bulk spin $\langle\sigma_k^z\rangle$ (plotted for $k = 2$, 50, and 99) decays rapidly to zero and no symmetry breaking is observed. This is the defining feature of the FSPT phase: time-translation symmetry only breaks at the boundary, not in the bulk. **b**. Fourier spectra of $\langle\sigma_k\rangle$. We find that $\sigma_1(\omega)$ and $\sigma_{100}(\omega)$ (which are on top of each other, so that $k = 1$ is not visible) have a peak at $\omega/\omega_0 = 1/2$, where $\omega_0 = 2\pi/T$ is the driving frequency. This peak is robust and rigidly locked to $\omega_0/2$, a manifestation of the robustness of the FSPT phase. For bulk spins, there is no such peak, consistent with no symmetry breaking in the bulk. **c**. Logarithmic entanglement entropy (abbreviated as "Ent. Entropy") growth. In the FSPT phase, the system is many-body localized. We thus expect logarithmic entanglement growth, which is shown in this figure. The entanglement has an initial quick rise until time $t \sim 1/J$. This initial rise corresponds to the expansion of wave packets to a size on the order of the localization length.

main text:

$$H(t) = \begin{cases} H_1, & 0 \le t < T_1 \\ H_2, & T_1 \le t < T \end{cases}, \tag{S7}$$

$$H_1 \equiv (\frac{\pi}{2} - \delta) \sum_k \hat{\sigma}_k^x, \tag{S8}$$

$$H_2 \equiv -\sum_k [J_k \hat{\sigma}_{k-1}^z \hat{\sigma}_k^x \hat{\sigma}_{k+1}^z + V_k \hat{\sigma}_k^x \hat{\sigma}_{k+1}^x + h_k \hat{\sigma}_k^x] \tag{S9}$$

where $T = 2T_1 = 2$.

Let us begin with the perfect case, where $\delta = 0$ and $V_k = h_k = 0$. The energy spectrum of H_2 is then perfectly four-fold degenerate. The eigenstates can be divided into four groups, i.e. $\{|A_k\rangle = |\uparrow \ldots \uparrow\rangle\}$, $\{|B_k\rangle = |\downarrow \ldots \uparrow\rangle\}$, $\{|C_k\rangle = |\uparrow \ldots \downarrow\rangle\}$, $\{|D_k\rangle = |\downarrow \ldots \downarrow\rangle\}$ with $E_{A_k} = E_{B_k} = E_{C_k} = E_{D_k}$. There exists a local effective free spin at each boundary. Since the effect of $U_1 = e^{-i\pi/2 \sum_k \hat{\sigma}_k^x}$ is to perfectly flip the spins at all sites, we obtain the following properties of the Floquet operator $U_F = \exp(-iH_2) \exp(-i\pi/2 \sum_k \hat{\sigma}_k^x)$:

$$U_F |A_k\rangle = \exp(-iH_2) |D_k\rangle = \exp(-iE_{D_k}) |D_k\rangle, \tag{S10}$$

$$U_F |B_k\rangle = \exp(-iH_2) |C_k\rangle = \exp(-iE_{C_k}) |C_k\rangle, \tag{S11}$$

$$U_F |C_k\rangle = \exp(-iH_2) |B_k\rangle = \exp(-iE_{B_k}) |B_k\rangle, \tag{S12}$$

$$U_F |D_k\rangle = \exp(-iH_2) |A_k\rangle = \exp(-iE_{A_k}) |A_k\rangle. \tag{S13}$$

From this, we see that U_F mixes the states $|A_k\rangle$ and $|D_k\rangle$ and mixes the states $|B_k\rangle$ and $|C_k\rangle$. Within the subspace of $|A_k\rangle$ and $|D_k\rangle$, U_F has matrix form

$$\begin{bmatrix} 0 & \exp(-iE_{D_k}) \\ \exp(-iE_{A_k}) & 0 \end{bmatrix}. \tag{S14}$$

Within the subspace of $|B_k\rangle$ and $|C_k\rangle$, U_F has matrix form

$$\begin{bmatrix} 0 & \exp(-iE_{C_k}) \\ \exp(-iE_{B_k}) & 0 \end{bmatrix}. \tag{S15}$$

Therefore, in the subspace formed by $|A_k\rangle$, $|B_k\rangle$, $|C_k\rangle$, and $|D_k\rangle$, U_F has eigenvalues $\pm\exp[-i(E_{A_k} + E_{D_k})/2]$ and $\pm\exp[-i(E_{B_k} + E_{C_k})/2]$. Thus, the Floquet effective Hamiltonian has eigen-energies $(E_{A_k} + E_{D_k})/2$, $(E_{B_k} + E_{C_k})/2$, $(E_{A_k} + E_{D_k})/2 + \pi$, $(E_{B_k} + E_{C_k})/2 + \pi \mod 2\pi$. As the energy spectrum of H_2 is four-fold degenerate ($E_{A_k} = E_{B_k} = E_{C_k} = E_{D_k}$), the Floquet eigen-energies satisfy $(E_{A_k} + E_{D_k})/2 = (E_{B_k} + E_{C_k})/2$, $(E_{A_k} + E_{D_k})/2 + \pi = (E_{B_k} + E_{C_k})/2 + \pi$. Therefore, the original four-fold degeneracy breaks into two-fold degeneracy in the presence of the drive. This two-fold degeneracy is a remnant of the original topological order. As for the Floquet eigenstates, they are cat-like linear combinations of topological eigenstates: $|A_k\rangle \pm |D_k\rangle$ and $|B_k\rangle \pm |C_k\rangle$. The mutual information between the two boundary spins is $2 \log 2$, indicating that there are long-range correlations between the boundaries.

When we turn on the two-body terms and the one-body terms in H_2, but still keep the system deep in the topological phase ($J_k \gg h_k, V_k$), H_2 has four nearly degenerate eigenstates related by the symmetry operations. The effective free spin at each boundary becomes quasi-local. Under Floquet driving, the near-four-fold degeneracy breaks into near-two-fold degeneracy: $(E_{A_k} + E_{D_k})/2 \approx (E_{B_k} + E_{C_k})/2$, $(E_{A_k} + E_{D_k})/2 + \pi \approx (E_{B_k} + E_{C_k})/2 + \pi$. Similarly, the eigenstates of the Floquet unitary are still cat-like states, and thus time-translation symmetry breaking can occur in this case. The stability of the FSPT phase will be discussed in more detail in Sec. I B 4.

3. Dynamical properties of the FSPT phase

Next, we will consider the evolution of this system and explicitly demonstrate the behavior of the FSPT phase.

Let us start from a product state $|\psi_0\rangle = |\downarrow ... \uparrow\rangle$. Here ... denotes a product state of bulk spins. Because the sate of the boundary spins corresponds to the group $\{|B_k\rangle\}$, we can expand the initial state as $|\psi_0\rangle = \sum_k b_k |B_k\rangle$. Under the time evolution U_F for one driving period, we have

$$\begin{aligned} U_F |\psi_0\rangle &= \exp(-iH_2) \exp(-i\pi/2 \sum_j \hat{\sigma}_j^x) \sum_k b_k |B_k\rangle \\ &= \exp(-iH_2) \sum_k b_k |C_k\rangle \\ &= \sum_k b_k \exp(-iE_{C_k}) |C_k\rangle , \end{aligned} \tag{S16}$$

where $|B_k\rangle = |\downarrow ... \uparrow\rangle$, $|C_k\rangle = |\uparrow ... \downarrow\rangle$. So, if we measure the edge spins in the initial state, we have $\langle\psi_0| \hat{\sigma}_1^z |\psi_0\rangle = -1$, $\langle\psi_0| \hat{\sigma}_N^z |\psi_0\rangle = 1$. After one Floquet period, the state becomes $|\psi_1\rangle = \sum_k b_k \exp(-iE_{C_k}) |C_k\rangle$. Because $|C_k\rangle$ has definite boundary spin expectation values, we will get $\langle\psi_1| \hat{\sigma}_1^z |\psi_1\rangle = 1$, $\langle\psi_1| \hat{\sigma}_N^z |\psi_1\rangle = -1$. Similarly, after two Floquet periods, the state becomes $|\psi_2\rangle = \sum_k b_k \exp(-iE_{C_k} - iE_{B_k}) |B_k\rangle$, and $\langle\psi_2| \hat{\sigma}_1^z |\psi_2\rangle = -1$, $\langle\psi_2| \hat{\sigma}_N^z |\psi_2\rangle = 1$. Thus, we see the the edge spins exhibit breaking of the time-translation symmetry.

As for bulk spins, assume that one bulk spin $\hat{\sigma}_j^z$ has the following expectation value in the initial product state: $\langle\psi_0| \hat{\sigma}_j^z |\psi_0\rangle = 1$. Writing $|\psi_0\rangle$ in the $|B_k\rangle$ basis, we have

$$\langle\psi_0| \hat{\sigma}_j^z |\psi_0\rangle = \sum_{k,k'} b_k b_{k'}^* \langle B_{k'}| \hat{\sigma}_j^z |B_k\rangle = 1. \tag{S17}$$

Since the spins of $|C_k\rangle$ are opposite to the spins of $|B_k\rangle$ at all sites, we immediately have that

$$\sum_{k,k'} b_k b_{k'}^* \langle C_{k'}| \hat{\sigma}_j^z |C_k\rangle = -1. \tag{S18}$$

However, the expectation value of $\hat{\sigma}_j^z$ in state $|\psi_1\rangle$ can be expressed as

$$\langle\psi_1| \hat{\sigma}_j^z |\psi_1\rangle = \sum_{k,k'} b_k b_{k'}^* \exp(-iE_{C_k} + iE_{C_{k'}}) \langle C_{k'}| \hat{\sigma}_j^z |C_k\rangle . \tag{S19}$$

Comparing the last two equations, we see that, because of the extra phase factor $\exp\left(-iE_{C_k} + iE_{C_{k'}}\right)$ before each component, the $\hat{\sigma}_j^z$ will not have definite value after the Floquet time evolution and will decay to zero quickly after random averaging. Thus, bulk spins do not exhibit breaking of the time-translation symmetry.

The above derivations tell that, for our model, the edge spins exhibit discrete time-translation symmetry breaking, while bulk spins relax very fast. Thus, the time-translation symmetry breaking only occurs at the boundaries as showing in Fig. S1**a**. We stress the importance of topology here. It protects the edge spins, ensuring the robustness of the edge spins against local perturbations that respect the underlying symmetry.

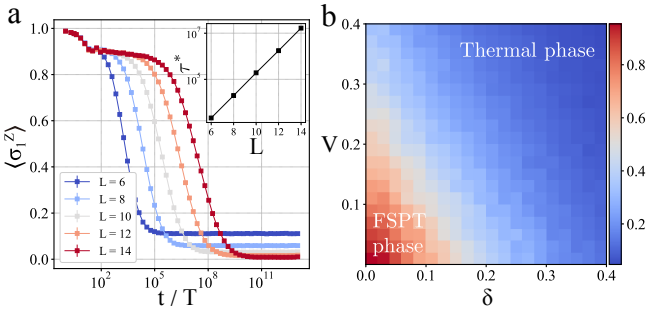

FIG. S2. The decay of boundary-spin magnetization and the phase diagram of the system. **a.** The decay of the first-spin magnetization, averaged over random disorder realizations. Here, the number of disorder realizations ranges from 3×10^4 ($L = 6$) to 10^3 ($L = 14$). The omitted parameters are chosen as in Fig. S1. We see an initial quick decay of $\langle\sigma_1^z\rangle$, followed by a plateau that extends up to a time diverging exponentially with system size. The inset shows the exponential scaling of τ^* with system size, where τ^* is the time when the edge spin decays to $1/2$. **b.** The phase diagram of the system as a function of the parameter δ in the definition of H_1 and the average strength V of the two-body interactions. Here, we adapt the string order parameter O_{sg} (averaged over 100 random realizations) as the indicator. It shows that when the imperfections are not very large, the string order parameter is approximately equal to one, indicating the topological phase. The other parameters are chosen as $J = \Delta J = 1$, $h = \Delta h = 0.01$.

Deep in the FSPT phase, the system represented by the static many-body-localized Hamiltonian H_2 has a complete set of quasi-local integrals of motion [S9]. Therefore, spins far away from each other can build significant entanglement only after exponentially long evolution time [S10]. Thus, under the Floquet time evolution, the entanglement entropy of our system exhibits logarithmic growth, as shown in Fig. S1**c**, and will eventually saturate to a value proportional to the system size.

Furthermore, when system size is finite, even deep in the topological phase, the Floquet time evolution will eventually lead to the decay of the spin signal at the boundaries. Indeed, the quasi-local effective free spins at the boundaries have tails that decay exponentially into the bulk. When system size is finite, these tails have an exponentially small overlap, which leads to the relaxation of the two effective free spins, with the lifetime diverging exponentially with system size. We demonstrate this phenomenon numerically in Fig. S2**a**.

4. The stability of the FSPT phase

The above considerations rely on the fact that, during each period, we perfectly flip spins at all sites. To show that the FSPT phase is indeed stable, we should make sure its defin-

ing properties hold even for an imperfect drive. We follow arguments similar to those introduced in Ref. [S5].

We showed above that, in the perfect-drive case ($\delta = 0$), the eigenstates of the Floquet evolution operator are cat-like states $|\psi_\pm^{AD}\rangle = |A_k\rangle \pm |D_k\rangle$ and $|\psi_\pm^{BC}\rangle = |B_k\rangle \pm |C_k\rangle$. We say that an effective short-range correlated topological state satisfies $\langle\psi|\,\hat{\sigma}_1\hat{\sigma}_N\,|\psi\rangle - \langle\psi|\,\hat{\sigma}_1\,|\psi\rangle\,\langle\psi|\,\hat{\sigma}_N\,|\psi\rangle \to 0$. Obviously, $|A_k\rangle, |B_k\rangle, |C_k\rangle, |D_k\rangle$ are short-range correlated topological states, but the Floquet eigenstates $|\psi_\pm^{AD}\rangle$ and $|\psi_\pm^{BC}\rangle$ are all long-range correlated, with different quasienergies. Then, any experimentally prepared short-range correlated state (such as a product state) can only be formed by taking a superposition of those long-range-correlated Floquet eigenstates with different quasienergies. Thus, after one period of Floquet evolution, local observables at the edge will not be invariant, signaling a breaking of discrete time-translation symmetry.

Now we add local $\mathbb{Z}_2 \times \mathbb{Z}_2$-symmetric perturbations into the system, such as an imperfect drive ($\delta \neq 0$), two-body interactions ($V_k \neq 0$), and single-body terms ($h_k \neq 0$). As long as the system is in an MBL phase, a local perturbation will significantly affect only nearby sites. Thus, we expect that the long-range correlations in the eigenstates of the Floquet unitary will not disappear. In fact, there exists a quasi-local $\mathbb{Z}_2 \times \mathbb{Z}_2$-symmetric unitary operator U, which constructs the perturbed Floquet eigenstates from the unperturbed Floquet eigenstates. Since U is quasi-local and symmetric, it cannot destroy the long-range boundary correlations of the unperturbed Floquet eigenstates. (Note, however, that perturbations that break the protecting symmetry but maintain MBL can destroy the FSPT phase, as discussed in Ref. [S11].) Therefore, time-translation-symmetry breaking can also occur in the locally perturbed system. To explicitly show that the FSPT phase is indeed a phase, we use the string order parameter O_{sg} as the indicator to plot in Fig. S2**b** the phase diagram with respect to the drive imperfection δ and the average strength V of two-body interactions.

5. *Mapping to free fermions when $V_k = 0$*

In this section, we review the mapping of the time-periodic Hamiltonian $H(t)$ defined in Eq. (1) in the main text [equivalently Eq. (S7)] to free fermions when the two-body interactions V_k are set to zero. This is achieved by a Jordan-Wigner transformation whereby a spin operator on site k is represented in terms of two Majorana operators, $\hat{\alpha}_k$ and $\hat{\beta}_k$. The Majorana operators are defined via the nonlocal mapping

$$\hat{\alpha}_k = \left(\prod_{j<k} \hat{\sigma}_j^x\right) \hat{\sigma}_k^z, \qquad \hat{\beta}_k = i\,\hat{\alpha}_k \hat{\sigma}_k^x. \tag{S20}$$

Under this transformation, we have

$$\hat{\sigma}_k^x = -i\hat{\alpha}_k\hat{\beta}_k \tag{S21a}$$

and

$$\hat{\sigma}_{k-1}^z \hat{\sigma}_k^x \hat{\sigma}_{k+1}^z = -i\hat{\beta}_{k-1}\hat{\alpha}_{k+1}. \tag{S21b}$$

The mapping thus results in redefined Hamiltonians

$$H_1 = -i(\frac{\pi}{2} - \delta) \sum_k \hat{\alpha}_k\hat{\beta}_k \tag{S22a}$$

and

$$H_2 = i \sum_k \left(J_k\,\hat{\beta}_{k-1}\hat{\alpha}_{k+1} + h_k\,\hat{\alpha}_k\hat{\beta}_k\right). \tag{S22b}$$

Note that H_2 can be rewritten as

$$\begin{aligned} H_2 &= H_2^{\text{odd}} + H_2^{\text{even}} \\ &= i \sum_{k\ \text{odd}} \left(J_{k+1}\,\hat{\beta}_k\hat{\alpha}_{k+2} + h_k\,\hat{\alpha}_k\hat{\beta}_k\right) \\ &\quad + i \sum_{k\ \text{even}} \left(J_{k+1}\,\hat{\beta}_k\hat{\alpha}_{k+2} + h_k\,\hat{\alpha}_k\hat{\beta}_k\right), \end{aligned} \tag{S23}$$

which corresponds to two decoupled Kitaev chains [S12], one on the odd and one on the even sublattice. The $\mathbb{Z}_2 \times \mathbb{Z}_2$ symmetry of $H(t)$ then manifests itself as the separate conservation of the two fermion parity operators

$$P_{\text{odd (even)}} = \prod_{k\ \text{odd (even)}} (i\hat{\alpha}_k\hat{\beta}_k), \tag{S24}$$

with eigenvalues ± 1.

When $T_1 = 1$ and $\delta = h_k = 0$, the time-dependent Hamiltonian $H(t)$ maps onto two copies of the fixed-point model for the nontrivial class D FSPT phase studied in Ref. [S13]. To see this, note that, when $\delta = 0$ and $T_1 = 1$, we have (up to an unimportant overall phase factor)

$$\exp\left(-iT_1H_1\right) = P_{\text{even}}P_{\text{odd}}. \tag{S25}$$

Thus, we obtain the Floquet operator (setting $T = 2T_1 = 2$)

$$U_F = P_{\text{even}}\, e^{-iH_2^{\text{even}}}\, P_{\text{odd}}\, e^{-iH_2^{\text{odd}}}. \tag{S26}$$

If we additionally set $h_k = 0$, this Floquet operator is just a product of two decoupled copies of the class D model considered in Ref. [S13]. The model studied in this work is thus expected to remain in this universality class for any small perturbations that respect the $\mathbb{Z}_2 \times \mathbb{Z}_2$ symmetry of Eq. (S26), including finite δ, h_k, and V_k.

II. DETAILS OF THE TEBD METHOD

We numerically simulate the time evolution process of the FSPT phase using the time-evolving block decimation (TEBD) method. This method was proposed for the time evolution of matrix product states (MPS) [S14, S15] and is a variant of the density matrix renormalization group (DMRG) algorithm [S16, S17]. At the heart of the TEBD method lies the

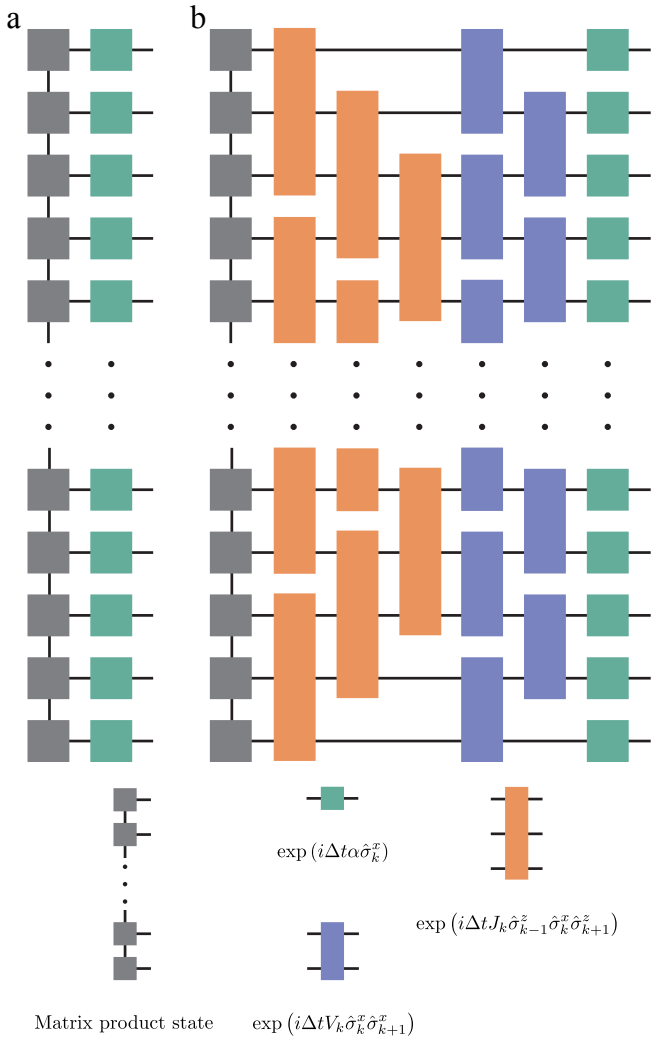

FIG. S3. Pictorial illustration of the implementation of the time-evolution unitary, where a connected wire between different blocks means contraction of indices. **a.** Implementation of $U_1(\Delta t)$. The gray blocks represent the current state in MPS form, and the green blocks represent the time evolution unitary consisting of one-body operators ($\alpha = -(\pi/2-\delta)$). **b.** Implementation of $U_2(\Delta t)$. The gray blocks represent the current state in MPS form; the orange blocks represent the time-evolution unitary consisting of three-body operators arranged in three groups; the blue blocks represent the time-evolution unitary consisting of two-body operators arranged in two groups; and the green blocks represent the time evolution unitary consisting of one-body operators ($\alpha = h_k$). These unitaries are applied to the the current state layer by layer.

Trotter-Suzuki decomposition of the time-evolution operator $U(\Delta t)$ of a short-range interacting system over a small time interval Δt. Usually, we can represent the operator $U(\Delta t)$ in the matrix-product-operator (MPO) form with small Trotter error, and then repeatedly apply it on the MPS representing the current state $|\psi(t)\rangle$ of the system to implement the time evolution.

Our FSPT phase has two distinct Hamiltonian operators in different time intervals as shown above. For the first time interval, the corresponding Hamiltonian is the sum of one-body operators on different sites. So the evolution operator is a direct product of one-body evolution operators

$$U_1(t) = e^{-itH_1} = e^{-it(\pi/2-\delta)\hat{\sigma}_1^x} \otimes ... \otimes e^{-it(\pi/2-\delta)\hat{\sigma}_k^x} \otimes ..., \tag{S27}$$

which can be represented as an MPO directly. To obtain the corresponding expectation values of local observables at different times, we also decompose the time evolution operator of an entire time interval T_1 into several small time intervals Δt. We show the implementation of $U_1(\Delta t)$ in Fig. S3**a**.

For the second time interval, the Hamiltonian H_2 consists of multiple short-range interaction terms: $H_2 = -\sum_k [J_k\hat{\sigma}_{k-1}^z\hat{\sigma}_k^x\hat{\sigma}_{k+1}^z + V_k\hat{\sigma}_k^x\hat{\sigma}_{k+1}^x + h_k\hat{\sigma}_k^x]$. Thus, we can approximate the time-evolution operator using Trotter-Suzuki decomposition $U_2(t) \approx [U_2(\Delta t)]^{t/\Delta t} = \left[e^{-i\Delta t H_2}\right]^{t/\Delta t}$ with $\Delta t \ll t$. To efficiently construct the MPO representation of $U_2(\Delta t)$, we group together terms in H_2 that commute with each other. The three-body operators are all stabilizer operators and commute with each other. For the two-body terms, they also commute with each other. For one-body terms, all of them are act on different sites and thus commute with each other. For simplicity, we denote $A = -\sum_k J_k\hat{\sigma}_{k-1}^z\hat{\sigma}_k^x\hat{\sigma}_{k+1}^z, B = -\sum_k V_k\hat{\sigma}_k^x\hat{\sigma}_{k+1}^x, C = -\sum_k h_k\hat{\sigma}_k^x$ and obtain

$$\begin{aligned} U_2(\Delta t) =& e^{-i\Delta t(A+B+C)} \\ =& e^{-i\Delta tC}e^{-i\Delta t(B+A)}e^{-i\Delta t^2[C,B+A]} \\ &+ \mathcal{O}(\Delta t^3) \\ =& e^{-i\Delta tC}e^{-i\Delta tB}e^{-i\Delta tA} + \mathcal{O}(\Delta t^2). \end{aligned} \tag{S28}$$

Thus, the time-evolution operator for H_2 over time interval t is approximated by

$$\begin{aligned} U(t) &\approx [U_2(\Delta t)]^{t/\Delta t} \\ &= \left(e^{-i\Delta tC}e^{-i\Delta tB}e^{-i\Delta tA}\right)^{t/\Delta t} + \mathcal{O}(\Delta t). \end{aligned} \tag{S29}$$

Furthermore, to make the numerical simulation more efficient, the implementation of three-body terms and the two-body terms can be accomplished layer by layer, wherein each layer only contains operators with nonoverlapping support, so that they can be applied to the MPS in parallel. We emphasize that, since the Trotter error is of order Δt, the time interval Δt should be small enough to avoid large TEBD error. The implementation of $U_2(\Delta t)$ is showed in Fig. S3**b**.

III. EXPERIMENTAL DETAILS

A. Quantum circuit ansatz

Algorithm 1: Neuroevolution Method

Output: Quantum circuit ansatz approximating target unitary.
Input: Elementary gate set $\mathcal{S}$, evolution unitary $U_2(\Delta t)$ and threshold β.
$\mathcal{G}$ = Direct_Graph($\mathcal{S}$);
$\mathcal{C}$ = Random_Generation_of_Quantum_Circuit($\mathcal{G}$);
$\mathcal{L}$ = Optimization($\mathcal{C}$, $U_2(\Delta t)$);
while $\min\{\mathcal{L}\} > \beta$ **do**
  $\mathcal{C}$ = Quantum_Circuit_Extension($\mathcal{C}$, $\mathcal{G}$);
  $\mathcal{L}$ = Optimization($\mathcal{C}$, $U_2(\Delta t)$);
end
return $\mathrm{argmin}_{\mathcal{C}}\{\mathcal{L}\}$;

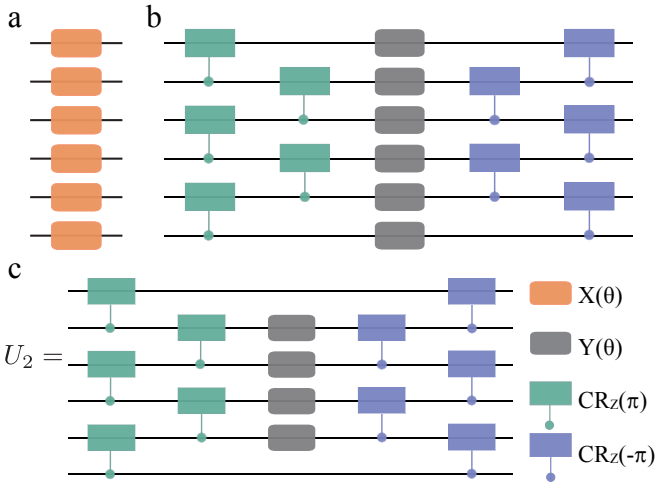

FIG. S4. Quantum circuit ansatzes used in our experiments. **a.** The circuit ansatz for the time-evolution unitary over the first time interval. **b.** The circuit ansatz for the time-evolution unitary over the second time interval, where the system is deep in the topological phase. **c.** The circuit ansatz for the time-evolution unitary over the second time interval, where the system contains no two-body operators and no one-body operators: $U_2 = \exp\left(i\sum_k J_k \hat{\sigma}^z_{k-1}\hat{\sigma}^x_k\hat{\sigma}^z_{k+1}\right)$.

Algorithm 2: Optimization for a quantum circuit

Output: Optimal parameters of the given quantum circuit.
Input: A quantum circuit C, evolution unitary $U_2(\Delta t)$ and learning rate γ.
Randomly initialize $\boldsymbol{\theta}$;
$U_{\text{circuit}}(\boldsymbol{\theta})$ = Unitary(C, $\boldsymbol{\theta}$);
$L = 1 - \mathrm{Tr}\left[U_2(\Delta t)^\dagger U_{\text{circuit}}(\boldsymbol{\theta})\right]/d$;
while $L > 0.001$ **do**
  $\boldsymbol{\theta} = \boldsymbol{\theta} - \gamma\nabla_{\boldsymbol{\theta}} L$;
  $U_{\text{circuit}}(\boldsymbol{\theta})$ = Unitary(C, $\boldsymbol{\theta}$);
  $L = 1 - \mathrm{Tr}\left[U_2(\Delta t)^\dagger U_{\text{circuit}}(\boldsymbol{\theta})\right]/d$;
end
return $\boldsymbol{\theta}$;

To observe the FSPT phase on a digital superconducting quantum computer, we need to decompose the time-evolution unitary into a quantum circuit consisting of a series of experimentally implementable quantum gates. Due to the direct-product structure of the evolution unitary $U_1(t) = e^{-itH_1}$ in the first time interval, this unitary can be represented as a quantum circuit using a layer of rotation gates along the x axis. Thus, it can be constructed and implemented relatively easily. As for the second time interval, the interaction among different sites takes the time-evolution unitary far away from a direct product form, making things a little different.

With the progress of research on variational quantum circuits, we are able to adapt this method to construct the quantum circuit of the second-time-interval unitary. Variational quantum circuits are a powerful tool that has been intensively investigated in recent years. Algorithms based on variational quantum circuits hold great potential in the noisy intermediate-scale quantum era. There are many algorithms based on variational parameterized quantum circuits, such as the variational quantum eigen-solver [S18], the quantum neural network [S19], etc.. The major distinction between standard quantum circuits and variational quantum circuits is that the gates composing a variational quantum circuit are not fixed. They can be modified by tuning their parameters using different parameter-updating algorithms. As these parameters are updated, the unitary implemented by the variational circuit is also updated. We terminate the updating procedure when a satisfactory result is obtained.

Our target is to find a variational quantum circuit, with some fine-tuned parameters, that approximates to high precision the evolution unitary $U_2(t) = e^{-itH_2}$ in the second time interval. We accomplish this target in two steps: find an implementable variational quantum circuit ansatz that can be used to represent the target unitary and keep updating the parameters contained in this circuit ansatz to find a good approximation of the desired unitary.

We use the neuroevolution method [S20] to find a suitable variational circuit architecture. The elementary gates used in our experiments are variable-angle single-qubit rotation gates, $X(\theta)$, $Y(\theta)$, $Z(\theta)$ (θ is the variational parameter), and a variable-angle control-rotation gate along the z axis $\mathrm{CR}_z(\theta)$ (θ is the variational parameter). Each of these gates contains a variational parameter, the rotation angle. These gates can form various quantum circuit layers. i.e. quantum circuits with depth equal to one. Using the method of

Ref. [S20], we construct out of these layers a directed graph, so that a quantum circuit can be represented as a path in this graph. To find the desired circuit, we follow the following procedure: 1) Randomly generate several variational quantum circuits of fixed depth based on the directed graph; 2) Update parameters contained in those quantum circuits using a gradient-based algorithm to minimize the loss function $L(\boldsymbol{\theta}) = 1 - \mathrm{Tr}\left[U_2(\Delta t)^\dagger U_{\text{circuit}}(\boldsymbol{\theta})\right]/d$, where $U_2(\Delta t)$ is the evolution unitary over the second time interval, $U_{\text{circuit}}(\boldsymbol{\theta})$ is the unitary represented by the current quantum circuit with variational parameters $\boldsymbol{\theta}$, and d is the dimension of the corresponding Hilbert space; 3) Chose quantum circuits with small values of the loss function and extend them based on the directed graph to generate new circuits; 4) Iterate processes 2) and 3) until the loss function is below a desired threshold. The circuit ansatz giving the smallest value of the loss function is regarded as the optimal ansatz representing the evolution unitary and is adapted in our experiments. We show the pseudo-code of this algorithm in Algorithm 1.

The quantum circuit ansatzes used in our experiments are shown in Fig. S4. We notice that the quantum circuit for the evolution unitary over the second time interval has a sandwich form $U_2(\Delta t) \approx WD(\boldsymbol{\theta})W^\dagger$, where $D(\boldsymbol{\theta})$ is a layer of single-qubit rotation gates with $\boldsymbol{\theta}$ being the evolution-time-dependent parameters. We note that the circuit structure in Fig. S4 **b** has an appealing merit: imagining that we first use this circuit to simulate the evolution the system under H_2 for a small time interval Δt, then for the subsequent time interval Δt the $\mathrm{CR}_z(\pi)$ gates in the corresponding circuit will cancel with the $\mathrm{CR}_z(-\pi)$ gates in the preceding circuit. As a result, for $2\Delta t$ time evolution the circuit maintains the same structure and we only need to double the angles for the single-qubit $Y(\theta)$ rotations to simulate the evolution. Thus, for one driving period the depth of the corresponding quantum circuit can be maintained to be six. We mention that this merit carries over to the circuit structure in Fig. S4 **c** as well.

With this circuit ansatz in hand, we can then use it to construct the circuits for our experiments. For a particular disorder realization of H_2 deep in the topological phase ($J_k \gg V_k, h_k$), we begin with this ansatz containing randomly generated variational parameters $\boldsymbol{\theta}$. The the gradient of the loss function $L(\boldsymbol{\theta})$ with respect to those variational parameters is computed and is used to update the current parameters $\boldsymbol{\theta}^{(n+1)} = \boldsymbol{\theta}^{(n)} - \gamma \nabla_{\boldsymbol{\theta}^{(n)}} L$, where γ is a given learning rate (we usually chose $0.001 \leq \gamma \leq 0.01$). In our calculation, we iterate this optimization procedure until the operator fidelity [S21] satisfies $\mathrm{Tr}\left[U_2(\Delta t)^\dagger U_{\text{circuit}}(\boldsymbol{\theta})\right]/d \geq 0.999$ ($L(\boldsymbol{\theta}) \leq 0.001$). We then take the quantum circuit with the final parameters as the approximation of the evolution unitary $U_2(\Delta t)$ in our experiments. We show the pseudo-code of this algorithm in Algorithm 2.

We emphasize that this optimization procedure is suitable for small systems. On the other hand, because of the exponential growth of the dimension of the Hilbert space, the optimization for large systems is impractical. It is helpful that the quantum circuit ansatz found using the neuroevolution method can exactly represent the evolution unitary $U_2(t) = e^{-itH_2}$ when H_2 has no two-body operators and no one-body operators (as shown in Fig. S4**c**). This indicates that we can analytically construct the corresponding quantum circuits for arbitrarily many qubits when $V_k = h_k = 0$, regardless of what values J_k and δ have. In fact, in this case, we can find an exact simple one-to-one mapping between J_k and the variational rotation angles in Fig. S4**c**. In our simulations and experiments, for systems of $L \leq 8$, the two-body terms and one-body terms are considered and the parameters in the corresponding quantum circuits are obtained using the above-described gradient-based optimization method. For 14-qubit systems, we only consider the stabilizer terms in H_2 and exactly construct the corresponding quantum circuits.

B. Device overview and measurement setup

To illustrate the idea of the FSPT phase, we select a chain of up to $L = 14$ qubits in a superconducting quantum processor, which is a flip-chip device hosting an array of 6×6 qubits distributed in a square lattice. To realize high-fidelity controlled-Z (CZ) gates, we adopt the tunable-coupler architecture [S22] to mediated nearest-neighbor qubit-qubit interactions, i.e., individual couplers are inserted between neighboring qubits with the qubit-coupler coupling strengths designed to be around 130 MHz for qubits at 6.5 GHz. All qubits (couplers) are of transmon type, with anharmonicities around 250 (350) MHz and maximum resonance frequencies around 7 (10.5) GHz. Each qubit has its own control line, which takes microwave (XY) inputs for rotating the qubit state around the x- or y-axis and flux-bias (Z) pulses for tuning the qubit frequency and rotating the qubit state around the z-axis; each coupler is frequency tunable via its own flux bias (Z) line, which guarantees that the effective coupling strength between two neighboring qubits at 6.5 GHz can be dynamically turned on, up to -25 MHz, or off, ≤ 0.25 MHz. Each qubit capacitively couples to its own readout resonator, designed in the frequency range from 4.1 to 4.4 GHz, for qubit state measurement. 9 readout resonators share one readout transmission line (TL) running across the processor chip, and 4 readout TLs can cover all 36 qubits in the processor.

The processor was fabricated using the flip-chip recipe: all qubits and couplers are located on the sapphire substrate (top chip); most of the control/readout lines and readout resonators are located on the silicon substrate (bottom chip). These two chips have lithographically defined base wirings, junction loops, and airbridges made of aluminum, and are galvanically connected via indium bumps with titanium under-bump metallization, as described elsewhere [S23]. The indium bumps were formed by the lift-off method with 9 μm-thick indium deposited on both chips, after which these two chips were aligned and bonded together at room temperature to complete the flip-chip device. The indium bumps in our processor are not only for ground connectivity, but also for passing through control signals from the bottom chip to the top chip where the

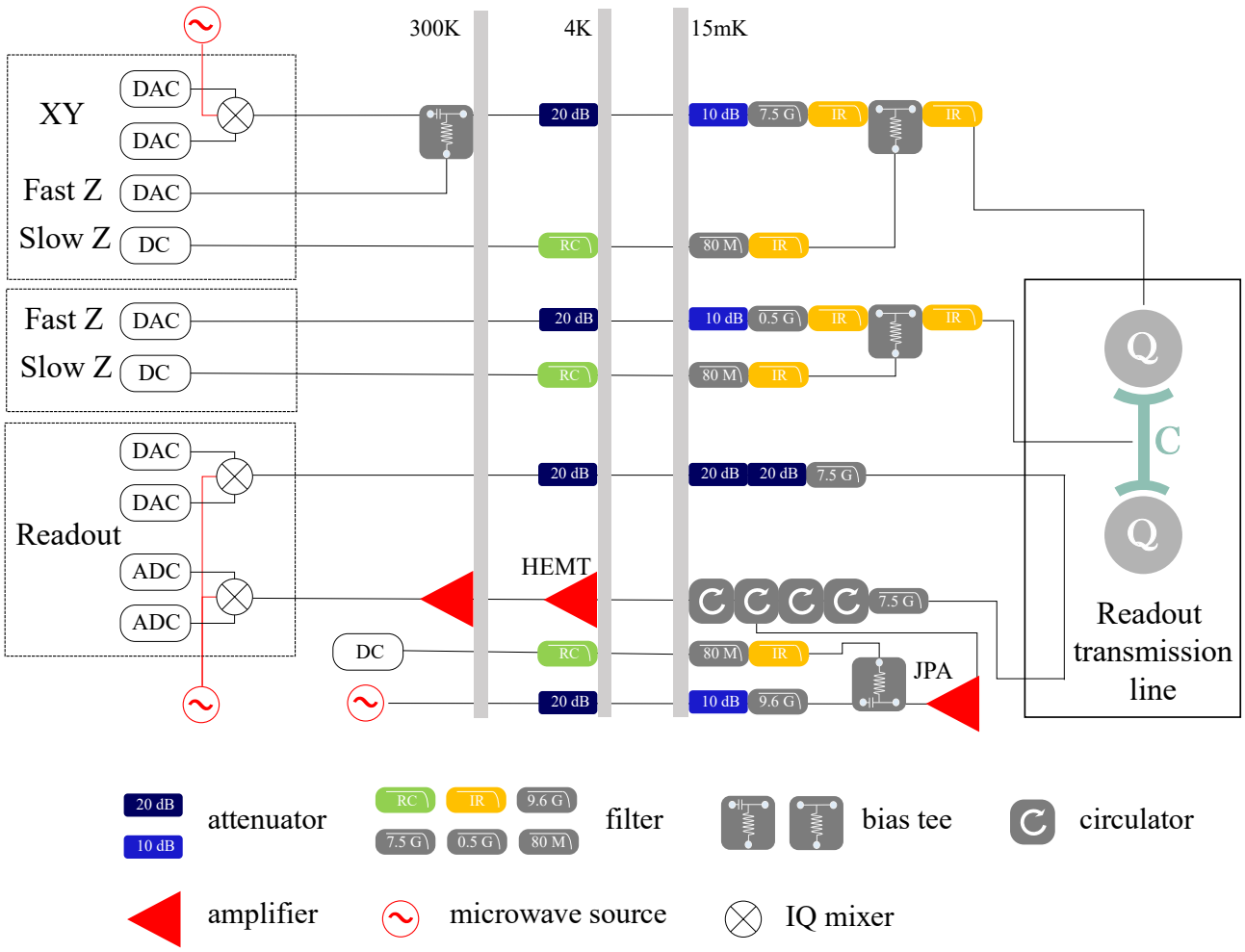

FIG. S5. Electronics and wiring setup illustrating how to synthesize and transmit the control/readout signals. Each qubit has three control channels: XY (microwave), fast Z (flux), and slow Z (flux). Each coupler has two control channels: fast Z and slow Z. Readout pulses are generated similarly to the XY signals and are passed through the processor via the readout TLs. All control and readout lines are well-attenuated and filtered for noise shielding and delicate control.

qubits are located.

The processor was loaded into a multilayer printed circuit board (PCB) enclosure, which was then mounted inside a dilution refrigerator (DR) with the base temperature down to 15 mK. Figure S5 shows the schematics of the control/readout electronics and wiring setup. In this setup, the XY microwave signals and fast Z pulses synthesized by digital-to-analog converters (DACs) are first joined together at room temperature, then attenuated and filtered at multiple cold stages of DR, and later combined with the slow Z (DC) pulses via home-made bias-tees at the mixing chamber stage of DR before being transmitted into the qubit control lines. The multiplexed readout signals are also heavily attenuated and filtered before going into the readout TLs of the processor to retrieve the qubit state information. To boost the signal-to-noise ratio (SNR), output signals from TLs are sequentially amplified by a Josephson parametric amplifier (JPA), a high electron mobility transistor (HEMT) amplifier, and room temperature (RT) amplifiers before being demodulated by analog-to-digital converters (ADCs) with 10-bit vertical resolution and 1.0 GS/s sampling rate. An arbitrary microwave signal can be generated by mixing the DAC outputs with continuous microwave using IQ mixer. DACs used to synthesize XY microwave signals and fast Z pulses in this experiment have 14-bit vertical resolution and 300 MHz output bandwidth. Slow Z (DC) pulses are generated by commercial 16-bit DACs with maximum outputs of ± 2.5 V.

C. Single- and Two-qubit gates

Single-qubit gates used in this experiment include X(θ), Y(θ), and Z(θ), which rotate the qubit state by an arbitrary angle θ around x-, y-, and z-axis, respectively. We realize X(θ) and Y(θ) by controlling the amplitude and phase of XY microwave pulses, and implement Z(θ) via the virtual Z gate [S24]. Single-qubit gate errors are characterized by simultaneous randomized benchmarking, yielding an average gate fidelity above 0.99 (see Tab. S1).

The basic structure to implement the CZ gate consists of two flux tunable qubits and one flux tunable coupler, which are, respectively, denoted as Q_1, Q_2, and C here for clarity of description. The effective coupling strength is composed of a direct coupling strength between two qubits and a part mediated by the coupler, which can be continuously adjusted by controlling the flux or frequency of the coupler. The Hamiltonian of this three body system is written as

$$\begin{aligned} H/\hbar = &\sum_{i=1,2,c} \omega_i a_i^\dagger a_i + \frac{\eta_i}{2} a_i^\dagger a_i^\dagger a_i a_i \\ &+ \sum_{i<j} g_{ij} \left(a_i - a_i^\dagger\right)\left(a_j - a_j^\dagger\right), \end{aligned} \tag{S30}$$

where $a_i^\dagger$ and a_i are raising and lowering operators, and g_{ij} is the coupling strength between each pair in $\{Q_1, Q_2, C\}$. The effective coupling strength between qubits is

$$\tilde{g} = g_{1c} g_{2c} \left(\frac{\omega_c}{\omega_1^2 - \omega_c^2} + \frac{\omega_c}{\omega_2^2 - \omega_c^2}\right) + g_{12}. \tag{S31}$$

In Fig. S6**a**, we plot the dynamic range of $\tilde{g}$ (bottom panel) processed using the two-qubit swap dynamics after initializing Q_1-Q_2 in $|10\rangle$, which shows that the effective coupling strength is tunable in the range from -25 MHz to ≤ 0.25 MHz. Experimentally, we can apply single-qubit gates while tuning the frequency of the coupler to around 10.5 GHz to turn off $\tilde{g}$.

To realize the CZ gate, we apply a flux bias (fast Z) pulse to steer the coupler's frequency along the following trajectory: 10.5→7.3→10.5 GHz. Meanwhile, we turn on the fast Z pulses to bring a pair of qubits from their idle frequencies to the pair of values $\left(\omega_j^{\mathrm{A(B)}}, \omega_{j+1}^{\mathrm{A(B)}}\right)$ (see Tab. S1), chosen such that $|11\rangle$ and $|02\rangle$ in the two-qubit subspace have nearly the same energy. After a finite period for this diabatic interaction, a unitary two-qubit gate equivalent to a CZ gate up to trivial single-qubit phase factors can be obtained as

$$\begin{pmatrix} 1 & 0 & 0 & 0 \\ 0 & e^{i\phi_1} & 0 & 0 \\ 0 & 0 & e^{i\phi_2} & 0 \\ 0 & 0 & 0 & e^{i\phi_3} \end{pmatrix}. \tag{S32}$$

A sine-decorated square pulse with the amplitude $A = z_0 \times \left[1 - r + r \sin\left(\pi \frac{t}{t_{\mathrm{gate}}}\right)\right]$ is used for the coupler in order to minimize state leakage. Experimentally, we fix $r = 0.3$ and only fine-tune the parameter z_0. All pulses are digitally smoothed by convolving them via a Gaussian window with $\sigma = 2$ ns before applying our pulse calibration routines [S28]. The CZ gate pulse duration is 30 ns, and there are additional 5 ns padding times before and after the 30-ns gate in compensation for the finite small tails of the smoothed pulse.

Individual CZ gates are calibrated following the procedure below:

1. Optimize coupler Z bias amplitude for minimum state leakage: We initialize Q_1-Q_2 in $|11\rangle$ and fix their frequency detuning at $\omega_1 - \omega_2 \approx -2\pi \times 250$ MHz, following which we apply the sine-decorated square pulse with a total length of 40 ns to the coupler. We search for the optimized pulse amplitude z_0 which maximizes the $|1\rangle$-state population for Q_1, i.e., minimum state leakage. In Fig. S6**b**, we plot the whole landscape of state leakage as functions of the Z bias amplitudes of both the coupler and Q_1, where the black solid line indicates how we sweep the coupler Z pulse amplitude.

2. Optimize phase factors: We fix the coupler Z pulse and sweep Q_1's Z pulse amplitude using different initial states to calculate the three phase factors in Eq. (S32), aiming at the condition $\phi_3 - \phi_2 - \phi_1 = \pi$. The black dashed line in Fig. S6**b** shows the routine of how we sweep the qubit Z pulse amplitude. We apply virtual Z gates to remove the trivial single-qubit phases.

3. Fine-tune gate parameters according to randomized benchmarking: We choose the randomized benchmarking sequence fidelity as a goal function to optimize relevant gate parameters, including the Z pulse amplitudes of both qubits and the coupler, and the single-qubit phases. We use the Nelder-Mead method to speed up the parameter optimization process.

IV. DYNAMICS OF ENTANGLEMENT

Unlike thermal phases without disorder or Anderson localized phases without interaction, where entanglement grows ballistically [S29–S31] or saturates to an area law at long times, respectively, the entanglement entropy of an MBL system grows logarithmically and saturates to a volume law in the long-time limit [S10]. In our experiment, we also extract the entanglement dynamics, through a full quantum state tomography of the reduced density matrix describing one half of the system. In Fig. S7**a**, we plot the reduced density matrix ρ_{half} for a single random instance of the Hamiltonian at the end of one driving period. Using the tomographically extracted ρ_{half} at different times, we extract the desired information about entanglement growth for the FSPT phase. Our results are plotted in Fig. S7**b**. From this figure, it is clear that, in the thermal phase, entanglement grows quickly and saturates

TABLE S1. Device parameters calibrated during the experiment. ω_j^0 is the maximum frequency of Q_j at zero flux bias. ω_j is the idle frequency where we initialize Q_j in $|0\rangle$ and subsequently apply single-qubit gates. η_j is Q_j's anharmonicity, which is approximately a constant within the frequency range relevant to this experiment. $\left(\omega_j^{\mathrm{A\,(B)}}, \omega_{j+1}^{\mathrm{A\,(B)}}\right)$ is a list of two frequencies for two neighboring qubits in group A (group B), chosen such that $|11\rangle$ and $|02\rangle$ in the two-qubit subspace have nearly the same energy for a CZ gate; the CZ gates for qubit pairs in the same group A (B) are implemented simultaneously when executing the multilayer quantum circuit to simulate the FSPT phase. ω_j^{m} is the readout frequency of Q_j where we apply readout pulses to excite Q_j's readout resonator for quantum state measurement. ω_j^{r} is the resonant frequency of Q_j's readout resonator. $T_{1,j}$ and $T_{2,j}^*$ are the energy relaxation time and Ramsey dephasing time of Q_j, respectively. $F_{0,j}$ and $F_{1,j}$ are the readout fidelity values for Q_j prepared in $|0\rangle$ and $|1\rangle$, respectively; these fidelity values are used to correct raw probabilities to eliminate readout errors as done previously [S25]. e_{sq} lists the single-qubit gate errors obtained by simultaneous randomized benchmarking. $e_{\mathrm{CZ}}^{\mathrm{A(B)}}$ list the CZ gate errors obtained by both individual and simultaneous randomized benchmarking for qubit pairs in group A (B). We note that the qubit parameters may slowly drift over time [S26, S27].

Qubit	Q_1	Q_2	Q_3	Q_4	Q_5	Q_6	Q_7	Q_8	Q_9	Q_{10}	Q_{11}	Q_{12}	Q_{13}	Q_{14}
$\omega_j^0/2\pi$ (GHz)	7.021	6.970	7.000	6.864	6.840	7.028	6.819	6.879	6.770	6.854	6.818	6.962	6.925	6.970
$\omega_j/2\pi$ (GHz)	6.450	6.730	6.890	6.651	6.565	6.750	6.676	6.600	6.520	6.620	6.721	6.893	6.838	6.960
$\eta_j/2\pi$ (GHz)	0.230	0.248	0.248	0.242	0.255	0.239	0.288	0.247	0.251	0.246	0.241	0.250	0.247	0.252
$\left(\omega_j^{\mathrm{A}}, \omega_{j+1}^{\mathrm{A}}\right)/2\pi$ (GHz)	6.414, 6.656		6.893, 6.651		6.275, 6.516		6.632, 6.868		6.349, 6.585		6.717, 6.957		6.684, 6.920	
$\left(\omega_j^{\mathrm{B}}, \omega_{j+1}^{\mathrm{B}}\right)/2\pi$ (GHz)		6.667, 6.898		6.651, 6.412		6.894, 6.657		6.766, 6.528		6.485, 6.722		6.910, 6.676		
$\omega_j^{\mathrm{m}}/2\pi$ (GHz)	6.110	6.198	5.608	6.651	5.552	6.309	6.722	5.997	5.812	5.828	6.323	5.736	6.181	6.423
$\omega_j^{\mathrm{r}}/2\pi$ (GHz)	4.357	4.194	4.119	4.200	4.097	4.343	4.323	4.223	4.262	4.206	4.152	4.269	4.182	4.402
$T_{1,j}$ (μs)	25	22	28	36	11	27	27	30	22	33	25	37	13	29
$T_{2,j}^*$ (μs)	1.0	1.7	4.5	2.5	3.8	2.2	1.2	1.6	0.8	2.1	3.1	2.8	5.8	14.0
$F_{0,j}$	0.950	0.955	0.945	0.888	0.951	0.951	0.961	0.956	0.868	0.880	0.959	0.935	0.980	0.970
$F_{1,j}$	0.876	0.862	0.834	0.888	0.886	0.942	0.859	0.900	0.890	0.905	0.900	0.898	0.919	0.937
e_{sq} (%)	0.49	0.45	1.26	0.72	0.38	0.69	0.66	0.47	0.84	0.60	0.33	0.55	0.55	0.45
$e_{\mathrm{CZ}}^{\mathrm{A}}$ (%) (Indiv.)	1.06		0.22		1.79		0.74		0.99		0.37		1.09	
$e_{\mathrm{CZ}}^{\mathrm{B}}$ (%) (Indiv.)		0.29		1.24		0.59		1.77		0.78		1.68		
$e_{\mathrm{CZ}}^{\mathrm{A}}$ (%) (Simu.)	3.46		0.99		3.00		0.76		2.03		0.79		1.33	
$e_{\mathrm{CZ}}^{\mathrm{B}}$ (%) (Simu.)		0.76		0.51		0.81		2.29		0.97		2.05		

to a maximal volume law ($\sim \frac{L}{2}\ln 2$). In contrast, in the FSPT phase, entanglement grows much slower. Due to decoherence and other imperfections in our experiment, we are not able to observe the logarithmic growth of entanglement. This not only demands a significant improvement of gate fidelities and a substantial increase of the coherence time, but also a more efficient and scalable approach to measure entanglement for a many-body system.

[S1] A. Shapere and F. Wilczek, Phys. Rev. Lett. **109**, 160402 (2012).
[S2] F. Wilczek, Phys. Rev. Lett. **109**, 160401 (2012).
[S3] P. Bruno, Phys. Rev. Lett. **111**, 070402 (2013).
[S4] H. Watanabe and M. Oshikawa, Phys. Rev. Lett. **114**, 251603 (2015).
[S5] D. V. Else, B. Bauer, and C. Nayak, Phys. Rev. Lett. **117**, 090402 (2016).
[S6] N. Y. Yao, A. C. Potter, I.-D. Potirniche, and A. Vishwanath, Phys. Rev. Lett. **118**, 030401 (2017).
[S7] V. Khemani, A. Lazarides, R. Moessner, and S. L. Sondhi, Phys. Rev. Lett. **116**, 250401 (2016).
[S8] Y. Bahri, R. Vosk, E. Altman, and A. Vishwanath, Nat. Commun. **6**, 7341 (2015).
[S9] M. Serbyn, Z. Papić, and D. A. Abanin, Phys. Rev. Lett **111**, 127201 (2013).
[S10] J. H. Bardarson, F. Pollmann, and J. E. Moore, Phys. Rev. Lett. **109**, 017202 (2012).
[S11] C. W. von Keyserlingk, V. Khemani, and S. L. Sondhi, Phys. Rev. B **94**, 085112 (2016).
[S12] A. Y. Kitaev, Physics-Uspekhi **44**, 131 (2001).
[S13] C. W. von Keyserlingk and S. L. Sondhi, Phys. Rev. B **93**, 245145 (2016).

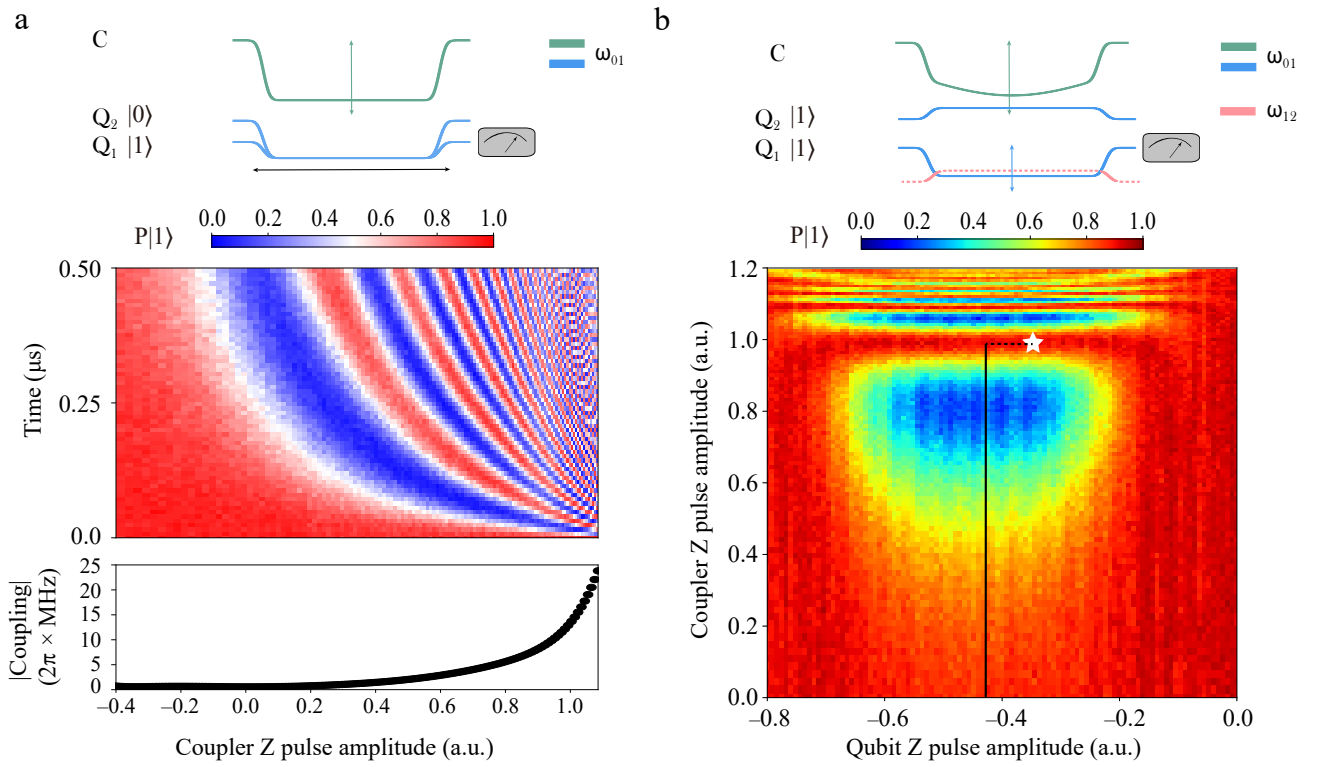

FIG. S6. Two-qubit CZ gate. **a**, two-qubit swap dynamics showing the dynamical range of the effective coupling strength as tuned by the coupler. **b**, $|1\rangle$-state population landscape for Q_1 resulting from the $|11\rangle$ and $|02\rangle$ interaction after initializing Q_1-Q_2 in $|11\rangle$. The white star marks the vicinity of the gate parameters used for the CZ gate, and lines indicate how we sweep Z parameters to approach this vicinity.

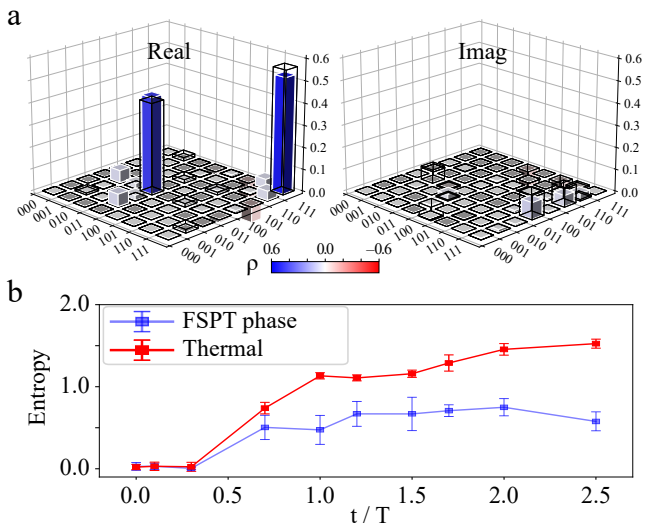

FIG. S7. Entanglement dynamics. **a**, Tomography of the reduced density matrix for the second half of a six-qubit chain after one driving period of one instance. The real and imaginary parts are shown in the left and right panel, respectively. **b**, Entanglement growth in both the thermal phase ($\delta = 0.65$, $J = 1$, $\Delta J = 0.05$ and $V = \Delta J = h = \Delta h = 0.01$) and the FSPT phase ($\delta = 0.01$, $J = \Delta J = 1$ and $V = \Delta J = h = \Delta h = 0.01$), averaged over 9 instances.

[S14] G. Vidal, Phys. Rev. Lett. **91**, 147902 (2003).
[S15] G. Vidal, Phys. Rev. Lett. **93**, 040502 (2004).
[S16] S. R. White and A. E. Feiguin, Phys. Rev. Lett. **93**, 076401 (2004).
[S17] A. J. Daley, C. Kollath, U. Schollwöck, and G. Vidal, J. Stat. Mech.: Theor. Exp. **2004**, P04005 (2004).
[S18] A. Peruzzo, J. McClean, P. Shadbolt, M.-H. Yung, X.-Q. Zhou, P. J. Love, A. Aspuru-Guzik, and J. L. O'Brien, Nat Commun. **5**, 4213 (2014).
[S19] K. Beer, D. Bondarenko, T. Farrelly, T. J. Osborne, R. Salzmann, D. Scheiermann, and R. Wolf, Nat. Commun. **11**, 808 (2020).
[S20] Z. Lu, P.-X. Shen, and D.-L. Deng, arXiv:2012.15131 (2020).
[S21] X. Wang, Z. Sun, and Z. D. Wang, Phys. Rev. A **79**, 012105 (2009).
[S22] F. Yan, P. Krantz, Y. Sung, M. Kjaergaard, D. L. Campbell, T. P. Orlando, S. Gustavsson, and W. D. Oliver, Phys. Rev. Appl. **10**, 054062 (2018).
[S23] K. Zhang, H. Li, P. Zhang, J. Yuan, J. Chen, W. Ren, Z. Wang, C. Song, D.-W. Wang, H. Wang, S. Zhu, G. S. Agarwal, and M. O. Scully, arXiv:2109.00964 (2021).
[S24] D. C. McKay, C. J. Wood, S. Sheldon, J. M. Chow, and J. M. Gambetta, Phys. Rev. A **96**, 022330 (2017).
[S25] Z. Wang, H. Li, W. Feng, X. Song, C. Song, W. Liu, Q. Guo, X. Zhang, H. Dong, D. Zheng, H. Wang, and D.-W. Wang, Phys. Rev. Lett. **124**, 013601 (2020).
[S26] P. V. Klimov, J. Kelly, Z. Chen, M. Neeley, A. Megrant, B. Burkett, R. Barends, K. Arya, B. Chiaro, Y. Chen,

A. Dunsworth, A. Fowler, B. Foxen, C. Gidney, M. Giustina, R. Graff, T. Huang, E. Jeffrey, E. Lucero, J. Y. Mutus, O. Naaman, C. Neill, C. Quintana, P. Roushan, D. Sank, A. Vainsencher, J. Wenner, T. C. White, S. Boixo, R. Babbush, V. N. Smelyanskiy, H. Neven, and J. M. Martinis, Phys. Rev. Lett. **121**, 090502 (2018).

[S27] W. Ren, W. Liu, C. Song, H. Li, Q. Guo, Z. Wang, D. Zheng, G. S. Agarwal, M. O. Scully, S.-Y. Zhu, H. Wang, and D.-W. Wang, Phys. Rev. Lett. **125**, 133601 (2020).

[S28] C. Song, K. Xu, W. Liu, C.-p. Yang, S.-B. Zheng, H. Deng, Q. Xie, K. Huang, Q. Guo, L. Zhang, P. Zhang, D. Xu, D. Zheng, X. Zhu, H. Wang, Y.-A. Chen, C.-Y. Lu, S. Han, and J.-W. Pan, Phys. Rev. Lett. **119**, 180511 (2017).

[S29] M. Cheneau, P. Barmettler, D. Poletti, M. Endres, P. Schauß, T. Fukuhara, C. Gross, I. Bloch, C. Kollath, and S. Kuhr, Nature **481**, 484 (2012).

[S30] P. Richerme, Z.-X. Gong, A. Lee, C. Senko, J. Smith, M. Foss-Feig, S. Michalakis, A. V. Gorshkov, and C. Monroe, Nature **511**, 198 (2014).

[S31] P. Jurcevic, B. Lanyon, P. Hauke, C. Hempel, P. Zoller, R. Blatt, C. Roos, *et al.*, Nature **511**, 202 (2014).